Ephemeris Monitor for GBAS Using Multiple Baseline Antennas with Experimental Validation

Samer Khanafseh, Jaymin Patel and Boris Pervan
Illinois Institute of Technology

BIOGRAPHY

Dr. Samer Khanafseh is currently a research assistant professor at Illinois Institute of Technology (IIT), Chicago. He received his MSc and PhD degrees in Aerospace Engineering from IIT in 2003 and 2008, respectively. Dr. Khanafseh has been involved in several aviation applications such as Autonomous Airborne Refueling (AAR) of unmanned air vehicles, autonomous shipboard landing for NUCAS and JPALS programs and Ground Based Augmentation System (GBAS). His research interests are focused on high accuracy and high integrity navigation algorithms, cycle ambiguity resolution, high integrity applications, fault monitoring and robust estimation techniques. He was the recipient of the 2011 Institute of Navigation Early Achievement Award for his outstanding contributions to the integrity of carrier phase navigation systems.

Jaymin Patel is a PhD student at the Illinois Institute of Technology, whose research focuses on the design of high accuracy and high integrity navigation algorithms and fault monitoring, signal in space fault detection for Ground Based Augmentation Systems (GBAS). He obtained his B.S degree in mechatronics engineering from Ganpat University in India and M.E degree in mechanical and aerospace engineering from IIT.

Dr. Boris Pervan is a Professor of Mechanical and Aerospace Engineering at IIT, where he conducts research on high-integrity satellite navigation systems. Prof. Pervan received his B.S. from the University of Notre Dame, M.S. from the California Institute of Technology, and Ph.D. from Stanford University. Prior to joining the faculty at IIT, he was a spacecraft mission analyst at Hughes Space and Communications Group and was project leader at Stanford University for GPS LAAS research and development. He was the recipient of the Mechanical and Aerospace Dept. Excellence in Research Award (2007), IIT/Sigma Xi Excellence in University Research Award (2005), University Excellence in Teaching Award (2005), Ralph Barnett Mechanical and Aerospace Dept. Outstanding Teaching Award (2002, 2009), IEEE Aerospace and Electronic Systems Society M. Barry Carlton Award (1999), RTCA William E. Jackson Award (1996), Guggenheim Fellowship (Caltech 1987), and Albert J. Zahm Prize in Aeronautics (Notre Dame 1986). He is currently Editor of the ION journal Navigation.

ABSTRACT

In this paper, a new ground-based monitor is developed that instantaneously detects all types of orbit ephemeris faults in Ground Based Augmentation Systems (GBAS). Ephemeris faults result in spatial gradients that can be detected using differential GPS measurements across spatially separated ground antennas. The monitor utilizes both carrier phase and pseudorange code measurements from multiple baselines for fault detection. We show that the developed monitor performance exceeds the existing fault detection algorithms and is capable of supporting Category III precision approach and landing.

INTRODUCTION

GBAS is a safety-critical system that is intended to support all phases of approach, landing, departure, and surface operations at an airport. GBAS will include multiple, spatially separated GPS antennas at each Ground Facility (GF), primarily to detect and isolate receiver faults and also to reduce the ranging error by averaging measurements for a given satellite. Differential GPS measurements across antennas can be used to detect and isolate the presence of ionospheric and ephemeris failures that are hazardous to GBAS.

There are three types of orbit ephemeris failures [1]. Type B failures occur when the broadcast ephemeris data is incorrect but no satellite maneuver is involved. Type A1 failures occur when the broadcast ephemeris data has been updated incorrectly following a satellite maneuver; a type A2 failure exists if the broadcast ephemeris remains unchanged after the maneuver. Type B failures can be detected by comparing the current ephemeris with a previously validated broadcast ephemeris [2]. In contrast,

previous ephemerides provide no benefit for the detection of type A1 and type A2 faults due to the presence of the satellite maneuver. In order to detect these faults, ground monitors based on the range and range rate of the satellite are utilized [1].

A major limitation of the range and range rate monitors is that their performance cannot be assessed analytically. Instead, Monte Carlo simulation is required to verify that the monitors meet requirements placed on the probability of missed detection. The fact that Monte Carlo methods are based on statistical samples weakens their ability to provide a persuasive case for integrity. In previous work, we proposed using the null space monitor, which takes a different approach to ephemeris fault detection by operating directly on raw GPS measurements [3,4]. Although we showed that the null space monitor can detect all orbit ephemeris faults regardless of type (A1, A2 or B), in order to achieve CAT III requirements, the monitor required 7 antennas. Installing 7 antennas in GBAS facilities will be costly and not feasible given regulatory siting constraints. In this work, we develop a detection algorithm that uses code and carrier phase measurements and requires less number of antennas. This has been achieved by filtering the code and carrier measurements to resolve the integer ambiguities, which are then used in the differential carrier phase test statistics.

The first section of this paper develops the carrier phase differential monitor that enables the detection of spatial gradients caused by orbit ephemeris faults. However, due to the presence of integer ambiguities in the carrier phase measurements, the range of detectable gradients is limited. In response, the following section of the paper develops a method to resolve the integer ambiguities and account for wrong cycle resolution. Next, we show the effect of the cycle resolution process on the monitor's false alarm and missed detection probabilities. The performance of this monitor is determined *a priori* through analytical means, which greatly facilitates the monitor design process. Data validations of the assumed simulation parameters and error models are presented in Appendix-A.

DIFFERENTIAL CARRIER PHASE MONITOR

Given that the likelihood of two or more simultaneous ephemeris faults is much smaller than the integrity risk requirement, GBAS presumes that only one satellite is affected by an ephemeris fault at any given time. For a faulty satellite *i* and a fault free satellite *j*, the differential carrier phase measurement for antenna 1 is

$$\begin{aligned}\Delta\phi_1 &= \left(r_1^i - r_1^j + \Delta I + \Delta T + \delta t_s\right) + \lambda\Delta n_1 + \Delta v_1 \\ &= \tilde{r} + \lambda\Delta n_1 + \Delta v_{\phi 1}\end{aligned} \tag{1}$$

where r_1^i and r_1^j are the ranges between antenna 1 and satellite *i* and *j*, respectively, ΔI is the single difference ionospheric error, ΔT is the single difference tropospheric error, δt_s is the single difference satellite clock bias, λ is the carrier wavelength, Δn_1 is the single difference cycle ambiguity for antenna 1 and $\Delta v_{\phi 1}$ is the single difference measurement error for antenna 1.

Similarly, the differential carrier phase measurement for antenna 2 can be written as

$$\begin{aligned}\Delta\phi_2 &= \left(r_2^i - r_2^j + \Delta I + \Delta T + \delta t_s\right) + \lambda\Delta n_2 + \Delta v_{\phi 2} \\ &= \tilde{r} + \left(r_2^i - r_1^i\right) - \left(r_2^j - r_1^j\right) + \lambda\Delta n_2 + \Delta v_{\phi 2}\end{aligned} \tag{2}$$

The differential range between the two antennas $\left(r_2^i - r_1^i\right)$ is equal to the dot product of the true differential line of sight unit vector from antenna 1 to satellite *i* ($\mathbf{e}_{i,true}^T$) and the baseline position vector between the two antennas ($\mathbf{b}_{12}$). Because satellite *i* is assumed to be faulty, the line of sight unit vector computed from the ephemeris ($\mathbf{e}_{i,eph}^T$) is faulted. Therefore

$$r_2^i - r_1^i = \mathbf{e}_{i,true}^T\mathbf{b}_{12} = \left(\mathbf{e}_{i,eph}^T + \delta\mathbf{e}_i^T\right)\mathbf{b}_{12} \tag{3}$$

where $\delta\mathbf{e}_i^T$ is the 3×1 ephemeris fault vector and $\mathbf{b}_{12}$ is the 3×1 relative position vector between antennas 1 and 2 expressed in the local North-East-Down (NED) frame.

Since satellite *j* is assumed to be fault free, the true line of sight unit vector between antenna 1 and satellite *j* is equivalent to the vector computed from the ephemeris, i.e.,

$$r_2^j - r_1^j = \mathbf{e}_{j,true}^T\mathbf{b}_{12} = \mathbf{e}_{j,eph}^T\mathbf{b}_{12} \tag{4}$$

By substituting equations (3) and (4) into equation (2), the measurement received by antenna 2 can be expressed as

$$\begin{aligned}\Delta\phi_2 &= \tilde{r} + \mathbf{e}_{i,eph}^T\mathbf{b}_{12} + \delta\mathbf{e}_i^T\mathbf{b}_{12} - \mathbf{e}_{j,eph}^T\mathbf{b}_{12} + \lambda\Delta n_2 + \Delta v_{\phi 2} \\ &= \tilde{r} + \Delta\mathbf{e}^T\mathbf{b}_{12} + \mathbf{b}_{12}^T\delta\mathbf{e}_i + \lambda\Delta n_2 + \Delta v_{\phi 2}\end{aligned} \tag{5}$$

where $\Delta\mathbf{e}^T = \mathbf{e}_{i,eph}^T - \mathbf{e}_{j,eph}^T$.

Taking the difference between two antennas (to form the double difference),

$$\begin{aligned}\Delta^2\phi_{12} &= \Delta\phi_2 - \Delta\phi_1 \\ &= \Delta\mathbf{e}^T\mathbf{b}_{12} + \mathbf{b}_{12}^T\delta\mathbf{e}_i + \lambda\Delta^2 n_{12} + \Delta v_{\phi 12}\end{aligned} \tag{6}$$

where $\Delta^2 n_{12} = \Delta n_2 - \Delta n_1$ is the double difference integer ambiguity, and Δv_{12} is the double difference carrier phase measurement error.

Assuming that the ambiguities are known, which will be discussed in the following section, the test statistic can be formed as,

$$q = \Delta^2\phi_{12} - \Delta e^T b_{12} - \lambda\Delta^2 n_{12} = \mathbf{b}_{12}^T\delta\mathbf{e}_i + \Delta v_{\phi 12} \tag{7}$$

Under fault-free conditions, the test statistic is normally distributed with a zero mean and the standard deviation as the double difference carrier phase measurement noise $\sigma_{\Delta^2\phi}$. Due to the low noise in the carrier phase measurements, the test statistic in (7) will be sensitive to Ephemeris faults, as we will show later. Next, we will address how to estimate and resolve the unknown cycle ambiguities.

CYCLE AMBIGUITY RESOLUTION

We will use the pseudorange measurements to estimate the cycle ambiguities, by differencing it from the carrier phase measurement:

$$z_{CMC} = \phi - \rho = \lambda n - 2I + v_\phi - v_\rho \tag{8}$$

The effect of ionospheric errors can be attenuated by taking the difference of z_{CMC} between two antennas (9).

$$\Delta z_{CMC_{12}} = z_{CMC_2} - z_{CMC_1} = \lambda\Delta n_{12} - 2\Delta I + \Delta v_\phi - \Delta v_\rho \tag{9}$$

The error in $\Delta z_{CMC_{12}}$ is dominated by thermal noise and multipath errors in Δv_ρ, which are much larger than the sub-cm level carrier phase noise or the 2-4mm/km differential ionospheric residual errors (vertical errors). Filtering $\Delta z_{CMC_{12}}$ reduces the effect of these errors and may allow resolving the integer ambiguity term Δn_{12} (10).

$$\Delta\hat{\mathbb{n}}_{12} = \frac{\sum \Delta z_{CMC_{12}}}{\mathbb{T}} = \Delta n_{12} + \varepsilon_{\Delta\hat{\mathbb{n}}} \tag{10}$$

where $\mathbb{T}$ is the estimated number of independent samples being averaged and

$$\varepsilon_{\Delta\hat{\mathbb{n}}} \sim N\left(0, \frac{\sigma_{zcmc}}{\sqrt{\mathbb{T}}}\right) \tag{11}$$

The float ambiguity estimate in (10) will not be sufficient to meet the requirements. The error in the float ambiguity estimate itself must be incorporated to the test statistic q in (7). One way to reduce the estimate error is by increasing the filtering period. But to reach the level of the carrier phase noise in q, and thus have minimal impact on the monitor's detection capabilities, filtering periods lasting hours would be necessary. Therefore, this approach is deemed not practical. Instead, the integer ambiguity can be computed by rounding the averaged value of $\Delta\hat{\mathbb{n}}$. The introduction of rounding means that the test statistic error will be the same as the carrier phase noise error (no impact). However, the rounding process, which is a nonlinear and may

result in the correct or incorrect integers, will cause the test statistic to be mixed gaussian distribution (Figure 1). Therefore, the likelihood of rounding to the wrong ambiguity must be accounted for. Recall that since z_{CMC} is fault free even under ephemeris fault, because it is geometry free by definition, the noise may cause the ambiguity to be rounded to the wrong integer. Under fault free conditions, a wrong ambiguity fix will cause the test statistic to be biased, which may cause a false alarm. Under the fault hypothesis, this incorrect fix may mask the actual fault, and thus causing a missed detection.

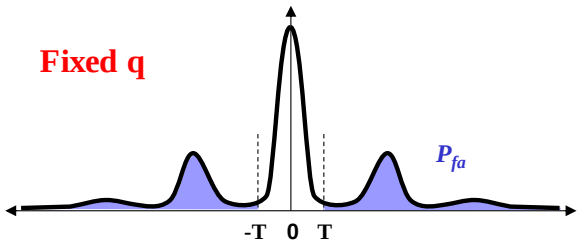

Figure 1: Illustration of the mixed Gaussian distribution of the test statistic q as a result of rounding

The probability of rounding to the correct ambiguity, or any specific incorrect one, can be computed from the Gaussian cumulative distribution function (CDF) given the distribution of $\varepsilon_{\Delta\hat{\mathbb{n}}}$ in (11). For example, Figure 2 highlights the regions corresponding to a correct fix and incorrect fixes of ± 1 integer cycle.

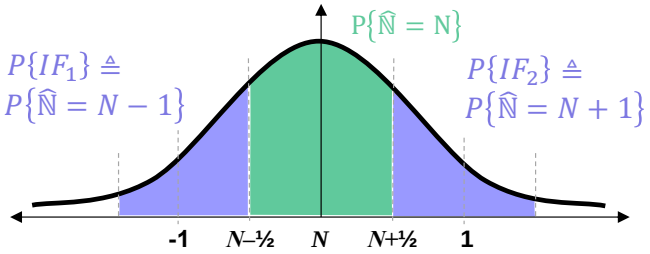

Figure 2: Example of cycle ambiguity correct and incorrect fix regions

Monitor False Alarm

It is practically not possible to integrate the mixed Gaussian distribution in Figure 1 to evaluate the false alarm probability. Given that the correct fix and all incorrect fix events are mutually exclusive and exhaustive events and using the total law of probability, we may express the false alarm probability under the null hypothesis H_0 (fault free) as

$$P_{fa} = P\{q > T|H_0\} = P\{q > T|H_0, CF\}P\{CF\} + P\{q > t|H_0, IF\}P\{IF\} \tag{12}$$

For simplicity, at this stage, we will conservatively assume that any incorrect fix event will result in a false alarm ($P\{q > t|H_0, IF\} = 1$). Since IF and CF events are mutually exclusive and exhaustive, $P\{IF\} = 1 - P\{CF\}$. As a result, the probability of false alarm in (12) can be bounded as

$$P_{fa} \leq P\{q > T|H_0, CF\}P\{CF\} + (1 - P\{CF\}) \tag{13}$$

Equation (13) illustrates that the probability of correct fix must be high enough such that the term $(1 - P\{CF\})$ is smaller than the allocated false alarm probability (in the order of 10^{-8} for GBAS CAT III). In order to achieve such probability, the float ambiguity estimate in (10) needs to be filtered for about an hour, which is not practical. Instead, we will provide a tighter bound on the false alarm probability in (13) by accounting for the impact of some incorrect fixes on the test statistic, while bounding the effect of the other incorrect fixes [5,6].

Incorrect fix events in (12) include infinite number of the mutually exclusive discrete incorrect fix events, and when expanded we can rewrite (12) as

$$P_{fa} = P\{q > T|H_0, CF\}P\{CF\} + \sum_{i=1}^{\infty} P\{q > T|H_0, IF_n\}P\{IF_n\} \tag{14}$$

Now, we will use the same bound technique as in (13), but only for a subset of the incorrect fixes $(n+1):\infty$ [6].

$$P_{fa} = P\{q > T|H_0, CF\}P\{CF\} + \sum_{i=1}^{n} P\{q > T|H_0, IF_n\}P\{IF_n\} + (1 - P\{CF\} - \sum_i^n P\{IF_n\}) \quad (15)$$

Even with the tight bound in (15) above, we needed to filter for prolonged periods before meeting the required level of P_{fa}. In response, we will introduce multiple threshold regions as illustrated in Figure 3. If the test statistic lies inside the regions corresponding to the correct fix, or the regions corresponding to ± 1 cycle ambiguity, no alarm is triggered. Equation (16) provides a mathematical definition of the threshold regions.

$$\{|q| > T\} \triangleq \{T < |q| < \lambda - T\} \cup \{|q| > \lambda + T\} \quad (16)$$

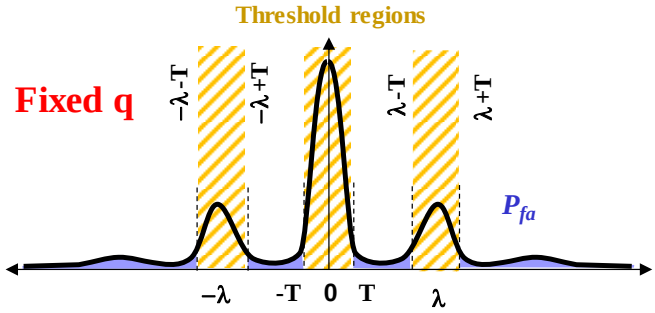

Figure 3: Illustration of the threshold regions defined in (16)

Using the definition in (16), we may rewrite P_{fa} in (15) as

$$P_{fa} = P\{q \succ T|H_0, CF\}P\{CF\} + \sum_{i=1}^{n} P\{q \succ T|H_0, IF_n\}P\{IF_n\} + (1 - P\{CF\} - \sum_i^n P\{IF_n\}) \quad (17)$$

Furthermore, we will utilize two aligned baselines with different lengths to improve the detection performance (Figure 4). In this configuration, the monitor will compute two different test statistics (one for each baseline length) and trigger an alarm if either test statistics exceeds the threshold regions (18).

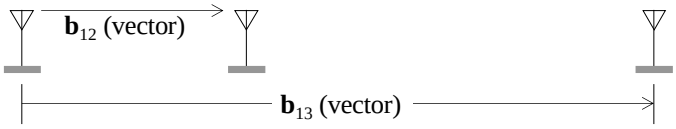

Figure 4: Illustration of two baselines used for detection

$$\begin{aligned} q_1 &= \Delta^2\phi_{12} - \Delta e^T b_{12} - \lambda\Delta^2 n_{12} = \mathbf{b}_{12}^T \delta\mathbf{e}_i + \Delta v_{\phi 12} \\ q_2 &= \Delta^2\phi_{13} - \Delta e^T b_{13} - \lambda\Delta^2 n_{13} = \mathbf{b}_{13}^T \delta\mathbf{e}_i + \Delta v_{\phi 13} \\ &if \quad \{q_1 \succ T\} \cup \{q_2 \succ T\} \quad \rightarrow \quad alarm \end{aligned} \quad (18)$$

Due to using the same antenna in both statistics, q_1 and q_2 will be correlated. The correlation, can be captured in the measurement noise covariance matrix. The monitor's test statistics become multidimensional mixed Gaussian distribution. Figure 5 illustrates a probability contour plot of the distribution and the threshold regions of such a monitor. The false alarm probability corresponds to the integration of the distribution over the non-highlighted regions. Mathematically, (17) becomes:

$$P_{fa} = P\{q_1 \succ T \cup q_2 \succ T\,|H_0\} = P\{q_1 \succ T|H_0\} + P\{q_2 \succ T|H_0\} - P\{q_1 \succ T \cap q_2 \succ T|H_0\} \quad (19)$$

Bounding the first two term in (19) can be carried out as shown in (17). The third term in (19) can bounded as,

$$P\{q_1 \succ T \cap\ q_2 \succ T\} \leq P\{q_1 \succ T \cap\ q_2 \succ T|CF_{1\cap2}\}P\{CF_{1\cap2}\} + \sum_{k=1}^{l} P\{q_{1k} \succ T \cap\ q_{2k} \succ T|IF_k\}P\{IF_k\}\ + \left(1 - P\{CF_{1\cap2}\} - \sum_{k=1}^{l} P\{IF_k\}\right) \quad (20)$$

Joint probability terms such as $P\{q_1 \succ T \cap q_2 \succ T\}$ or $P\{CF_{1\cap2}\}$ are computed numerically using the multivariate Gaussian joint probability function (*mvncdf* in MATLAB®, for example).

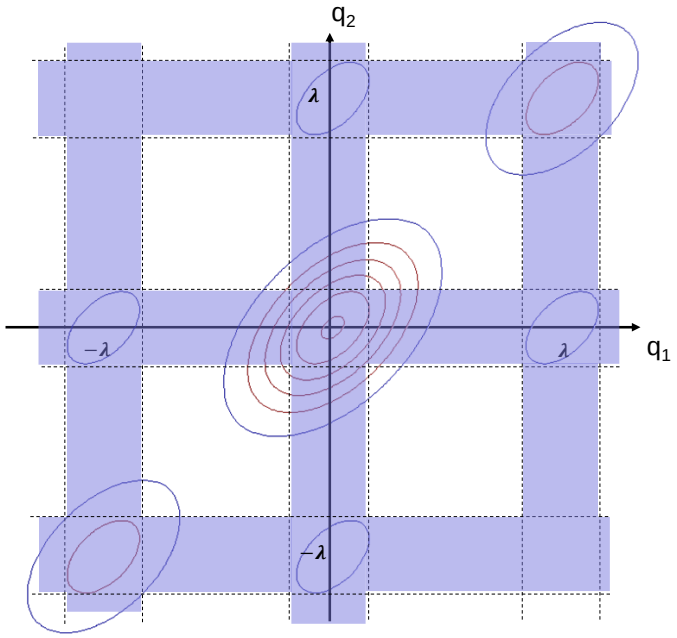

Figure 5: Contour plot showing the multivariate mixed Gaussian distribution corresponding to the multi-baseline monitor and the threshold regions

Given a specific false alarm budget and code and carrier error models, we use equations (11), (19) and (20) with the definition in (16) to solve for the filtering period and threshold.

Monitor Missed Detection

A missed detection will occur if both test statistics are inside the threshold regions under the fault hypothesis H_f (Figure 6).

$$P_{md} = P\{q_1 \prec T\ \cap\ q_2 \prec T\ |H_f\} \quad (21)$$

Similar to the false alarm probability in the previous subsection, (21) can be bounded as

$$P\{q_1 \prec T\ \cap\ q_2 \prec T\} \leq P\{q_1 \prec T\ \cap\ q_2 \prec T|CF_{1\cap2}\}P\{CF_{1\cap2}\} + \sum_{k=1}^{l} P\{q_{1k} \prec T \cap\ q_{2k} \prec T|IF_k\}P\{IF_k\}\ + \left(1 - P\{CF_{1\cap2}\} - \sum_{k=1}^{l} P\{IF_k\}\right) \quad (22)$$

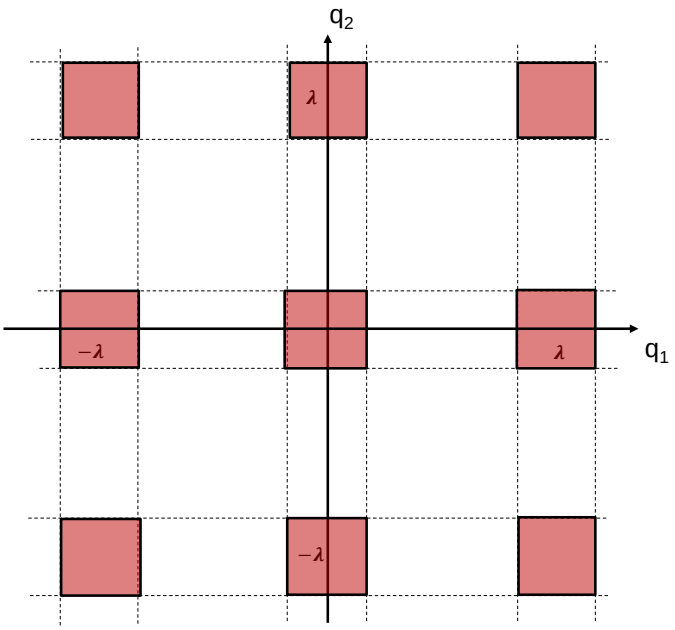

Figure 6: Missed detection regions for the multi-baseline monitor

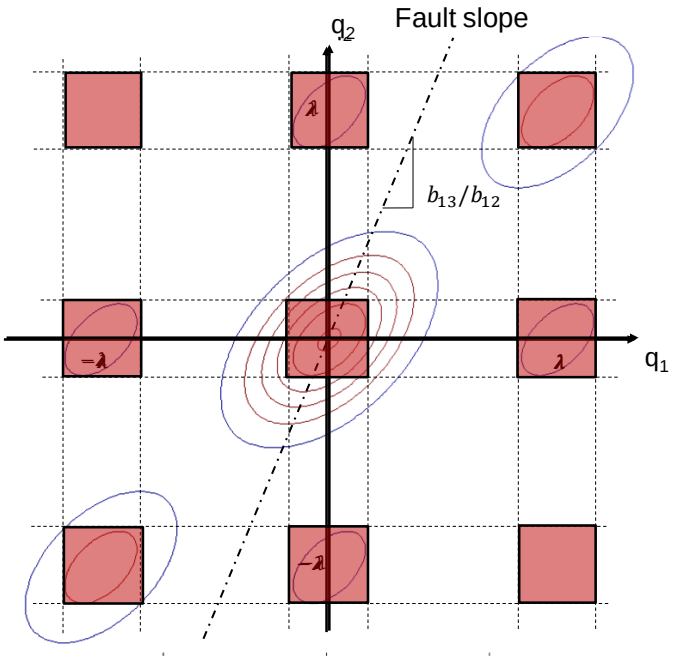

Figure 7: Contour plot showing the multivariate mixed Gaussian distribution corresponding to the multi-baseline monitor, the missed detection regions, and the fault slope

Under fault conditions, the "mean" (which corresponds to the maximum peak of the distribution) of the multivariate mixed Gaussian distribution will be moving along the fault slope as shown in Figure 7. It can be easily shown from (18) that the fault slope, which is the ratio of q_2/q_1, is equal to b_{13}/b_{12}. The figure illustrates that in order to minimize the probability of missed detection, the fault slope needs to avoid passing through the threshold regions. In future work, we will exploit this property to provide an optimal selection of baseline ratio or baseline lengths, given specific siting constraints.

MONITOR PERFORMANCE EVALUATION

In GBAS Approach Service Type D (GAST-D) CAT III, the current Standards and Recommended Practices (SARPs) has no requirements specifically placed on the ephemeris monitor. Two requirements apply to the post monitoring error in the corrected pseudorange, and are depicted in Figures 8 and 9 [7]. In both cases, the requirement applies to the probability of missed detection as a function of the size of the error due to the fault. The difference between the two requirements is whether or not there is a prior probability of a fault. Figure 8 represents the requirement without taking the fault prior probability into account. Figure 9 shows the P_{MD} requirements weighted by the prior probability. So, the difference is that in Figure 9, the P_{MD} performance curve from the monitor is weighted by the prior probability then sketched and compared to the highlighted area. The ephemeris monitor P_{MD} should satisfy both requirements.

The probability of false alarm is set to 10^{-8} to satisfy the continuity requirement. We also assume a 10^{-5} prior probability of ephemeris fault. Based on experimental analysis of data collected by the Federal Aviation Administration (FAA) Technical Center, it is shown in Appendix-A that the cumulative

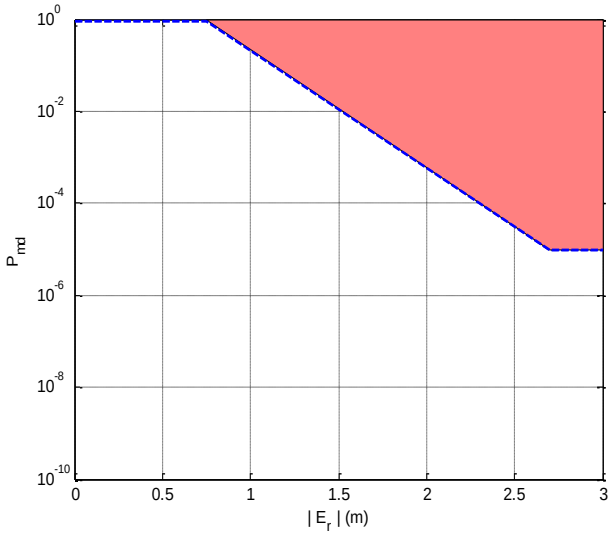

Figure 8: Requirement on probability of missed detection assuming no a priori knowledge of the probability of a fault.

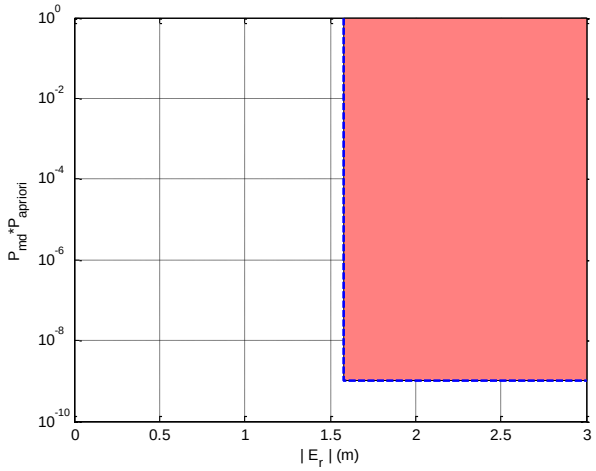

Figure 9: Requirement on probability of missed detection when a priori knowledge of the probability of a fault is available.

probability distribution of the double difference carrier phase measurement error can be overbounded by a zero-mean Gaussian distribution with a standard deviation of 6 mm, and the double difference pseudorange is bounded by a standard deviation of 83cm. The ionospheric error standard deviation of 4mm/km is assumed based on the results in [8], which is converted to a conservative range error using the obliquity factor for a satellite at 5 degree elevation.

After analyzing the data in Appendix-A, the time constant of the pseudorange was found to be 2sec. We assume that the reference satellite, which has been validated and tracked for far longer than the tested one, was filtered for 5400 seconds. Based on the false alarm analysis using Equations (11), (19) and (20), we needed a filtering period of 492 sec and threshold of 36.4mm was adequate to meet 10^{-8} using 200m and 700m long baselines.

Different ephemeris fault gradients have been simulated to evaluate P_{md}. For a 3° glide slope, the distance between the aircraft and reference antennas is 5 km at the decision height. Therefore, the ranging error resulting from an ephemeris fault is computed by multiplying the ephemeris fault gradient by the 5km distance. This process is then repeated for all tested gradient values. Figure 10 shows the resultant P_{md}, where the highlighted area illustrates the monitor requirements shown in Figure 9 after weighting by a prior probability of 10^{-5}. The red curve represents the minimum detectable ranging error for different probabilities of missed detection. It can be seen that this curve never penetrates the highlighted region, and hence the monitor satisfies the requirements. In contrast, if the ambiguities were not fixed and the float ambiguities after filtering for the same period of 492 seconds were used in the test statistics, the yellow curve in Figure 11 shows that the monitor doesn't meet the requirements.

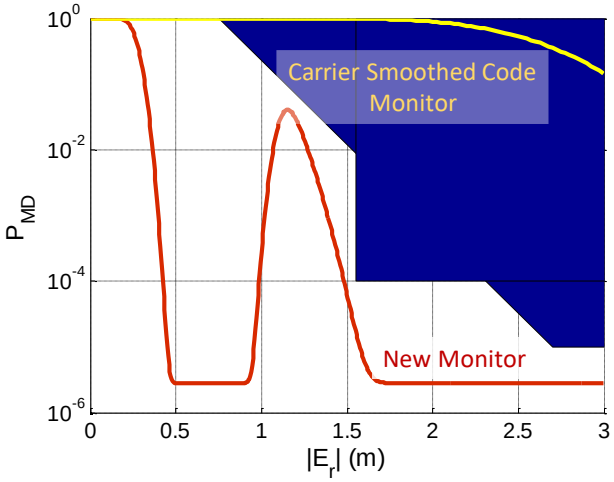

Figure 11: Pmd vs ranging error for an aircraft at 5km distance from the GBAS ground station. Red: new monitor using fixed ambiguities, Yellow: using float ambiguity (equivalent to carrier-smoothed-code).

In summary, using two baselines is sufficient to meet the GBAS CAT-III requirements. The results in this paper were based on a 1-D installation, meaning that the runway and antennas are parallel. The same concept can be extended to detect ephemeris faults with multiple runway facilities. It is expected that 4 baselines (with perpendicular two) will be sufficient to detect all ephemeris faults. This means that 5 antennas, not 7 as was concluded in our previous work [4] will be enough. Future work will demonstrate this capability in addition to investigating the impact of the 492 sec filtering period on GBAS availability, extend the monitor to multiple dimensions with baseline topology optimization, and extend the monitor to detect ionospheric faults.

CONCLUSION

In this paper, we introduced a new differential carrier phase based monitor that utilizes the pseudorange measurements to resolve the cycle ambiguities and extract the most of the carrier phase sensitivity to detect faults due to its low noise. The likelihood of wrong ambiguity fix is accounted for in evaluating the false alarm and missed detection probabilities. We showed that the ephemeris monitor introduced in this work can instantaneously detect all types of ephemeris faults (B, A1 and A2 type faults) while meeting the GBAS GAST-D CAT-III requirements. We also demonstrated that compared to other previously designed monitors, this monitor requires less antennas without sacrificing performance. Aspects including extension to detect ionospheric faults and antenna siting optimization will be addressed in the future.

ACKNOWLEDGEMENTS

The authors would like to thank the Federal Aviation Administration (FAA) for their continued support of this research effort. The opinions in this paper are our own and do not represent those of any other person or organization.

APPENDIX–A: EXPERIMENTAL VALIDATION

Raw pseudorange and carrier phase measurements were collected from four Low Multipath Antennas (LMA) located at the LAAS Test facility in Newark Liberty International Airport (EWR). LMA is an array antenna that rejects multipath while meeting the signal-to-noise ratio requirements at low elevation.

The characterization of pseudorange measurement error can be carried out in two ways: computing code minus carrier, or computing the double difference pseudorange residual. Since we rely on single differencing for ambiguity resolution, we opted for the double difference approach. Similar to the carrier phase residual development in (1) to (7), the double difference pseudorange residual error between two receivers, *k* and *l*, and two satellites, *i* and *j*, is computed using the lines of sight vectors (e_i and e_j) and baseline *b* as

$$r_{\Delta^2\rho} = \rho_k^i - \rho_l^i - \left(\rho_k^j - \rho_l^i\right) - \left(\Delta e_i - \Delta e_j\right) \cdot b = \varepsilon_{\Delta^2 \rho_{kl}^{ij}} \tag{A.1}$$

Figure A-1 shows the residual in (A.1) computed for 27-hour period of EWR data starting from hour 90.5 to 118 of Week 1887.

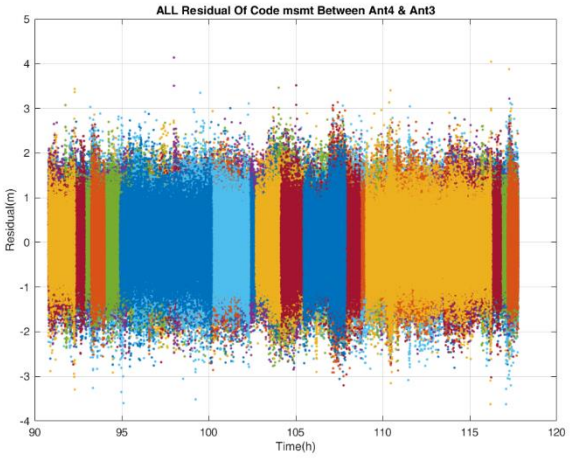

Figure A-1: Double difference pseudorange residual

We use the folded cumulative distribution function (folded-CDF) bounding method to evaluate the residual error models [9,10]. In folded CDF representation, the empirical CDF is computed for the data and then compared to a Gaussian CDF with specific mean and standard deviation. Folded in this context means that the left tail likelihood is computed for errors less than the median and the right tail likelihood is computed for the ones larger than the median. The Gaussian CDF with the mean and standard deviation values that overbound all empirical CDF points is referred to as the bounding Gaussian distribution, and will be used for error modeling. Figure A-2 shows the residual folded CDF and the bounding Gaussian with a standard deviation of 84cm (thick red line).

Similarly, double difference carrier phase measurement residuals are computed (Figure A-3). The residuals for the carrier phase LMA data shown in Figure A-3 is after correcting for antenna phase center as discussed in [11]. Figure A-4 shows that the carrier phase residuals are overbounded by Gaussian distribution with zero mean and standard deviation of 4.5mm (thick red line). Other baselines form the same set showed that a standard deviation of 84cm for pseudorange and 6mm for carrier phase errors.

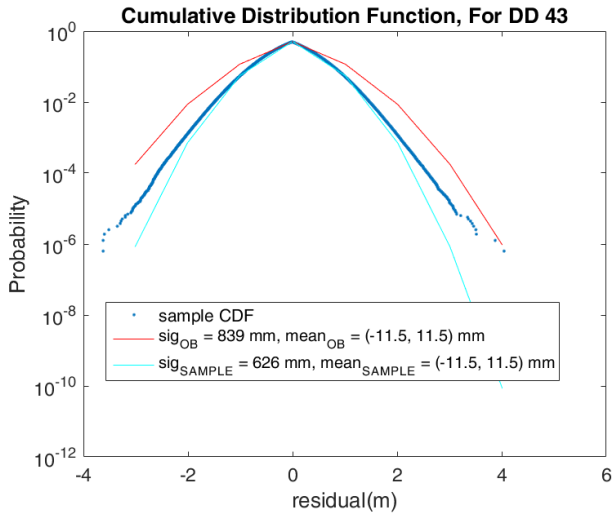

Figure A-2: Folded CDF bound for double difference pseudorange residuals

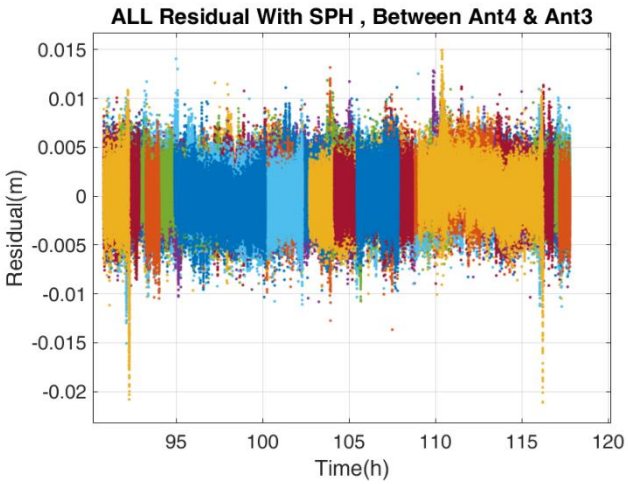

Figure A-3: Double difference carrier phase residuals

Next, we validate the time constant value used in filtering the carrier-minus-code CMC (9) and (10). Float ambiguity estimated by filtering the single difference CMC for 492 sec is computed and differenced from the "true ambiguities" (computed by postprocessed float ambiguities for all continuous passes). The results of this difference, which represents the filtered float ambiguity estimate error, are then plotted in a CDF bound curve like the one in Figure A-4. For the theoretical bound, we use a Gaussian CDF with a standard deviation corresponding to (11), which is repeated here for completeness.

$$\varepsilon_{\Delta\hat{\mathbb{m}}} \sim N\left(0, \frac{\sigma_{zcmc}}{\sqrt{\mathbb{T}}}\right) \tag{A.2}$$

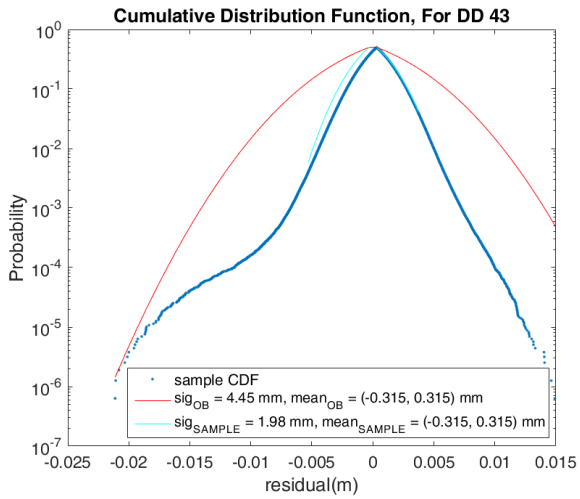

Figure A-4: Folded CDF bound for the double difference carrier phase residuals

We use the bounded standard deviation of pseudorange for σ_{zcmc} and solve for the time constant assuming that $\mathbb{T} = 492/2\tau$, where τ is the time constant and 492 correspond to the filtering period (we assume independence every two time constants). Then, we change the value of τ until the Gaussian theoretical CDF overbounds the estimated float ambiguity error. Figure A-5 shows that a time constant τ of 2 seconds for a filtering period of 492 seconds bounds the float ambiguity error.

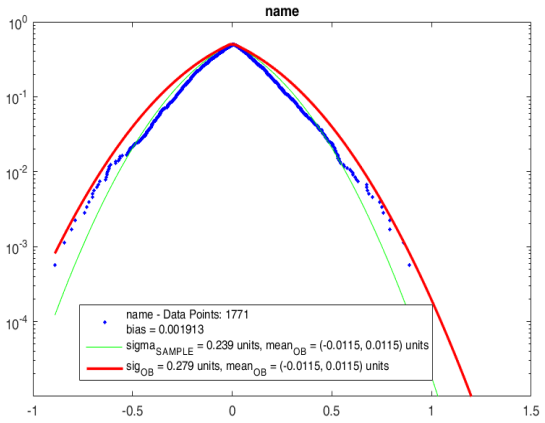

Figure A-5: Folded CDF bound for the filtered float ambiguity error

REFERENCES

[1] Tang, H., Pullen, S., Enge, P., Gratton, L., Pervan, B., Brenner, M., Scheitlin, J., Kline, P., "Ephemeris Type A Fault Analysis and Mitigation for LAAS," *Proceedings of IEEE/ION PLANS 2010*, Indian Wells, CA, May 2010, pp. 654-666.

[2] B. Pervan and L. Gratton. Orbit ephemeris monitors for local area differential gps. IEEE Transactions on Aerospace and Electronic Systems, 41.2, 2005.

[3] Jing, J., Khanafseh, S.K., Chan, F.-C., Langel, S., Pervan, B., "Detecting Ionospheric Gradients for GBAS Using A Null Space Monitor," Proceedings of IEEE/ION PLANS 2012, Myrtle Beach, South Carolina , April 2012, pp. 1125-1133.

[4] J. Jing, S. Khanafseh, S. Langel, F-C. Chan, and B. Pervan. "Null Space Ephemeris Monitor for GBAS". Proceedings of the ION 2013 Pacific PNT Meeting. Honolulu, HI. April 2013, pp. 978-985.

[5] S. Khanafseh and S. Langel, “Implementation and Experimental Validation of Cycle Ambiguity Resolution with Position Domain Integrity Risk Constraints,” NAVIGATION: Journal of the Institute of Navigation, Vol. 58, No. 1, Spring 2011, pp. 45-58.

[6] Samer Khanafseh and Boris Pervan, “A New Approach for Calculating Position Domain Integrity Risk for Cycle Resolution in Carrier Phase Navigation Systems,” IEEE Transaction on Aerospace and Electronic Systems, Vol. 46, No. 1, Jan. 2010

[7] Tim Murphy,Stefan Naerlich, "SARPs for GNSS Elements and Signals (GBAS),"Navigation Systems Panel (NSP) Working Group of the Whole Meeting, Montreal, 17 – 28 May 2010

[8] Lee, J., Pullen, S., Datta-Barua, S., and Enge, P., “Assessment of Ionosphere Spatial Decorrelation for Global Positioning System-Based Aircraft Landing Systems,” Journal of Aircraft, Vol. 44, No. 5, 2007, pp. 1662–1669

[9] B. DeCleene, “Defining Pseudorange Integrity - Overbounding,” Proceedings of the 13th International Technical Meeting of the Satellite Division of The Institute of Navigation (ION GPS 2000), Salt Lake City, UT, September 2000, pp. 1916-1924.

[10] J. Rife, S. Pullen, P. Enge, and B. Pervan, “Paired Overbounding for Nonideal LAAS and WAAS Error Distributions,” *IEEE Transactions on Aerospace and Electronic Systems,* Vol. 42, No. 4, October 2006, pp. 1386-1395.

[11] Gratton, L., Khanafseh, S., Pervan, B., and Warburton, J., “Experimental Observations and Integrity Monitor Applications of LAAS IMLA Carrier Phase Measurements,” Proceedings of the 17th International Technical Meeting of the Satellite Division of the Institute of Navigation (ION GNSS-2004), Long Beach, CA, September 21-24, 2004.

[12] Khanafseh, Samer, Pullen, Sam, Warburton, John, “Carrier Phase Ionospheric Gradient Ground Monitor for GBAS with Experimental Validation”, NAVIGATION, Vol. 59, No. 1, Spring 2012, pp. 51-60.